Semiconductor Optoelectronics, *Vol. 41 No. 11 (2022), 772-788*
https://bdtgd.cn/

DISPERSION RELATIONS OF CHIRAL METAMATERIAL SLAB WAVEGUIDE WITH GRAPHENE INTERFACES

Hawraa H. Salman
Physics Department, Science College, Thi-Qar University
hawraa_ham.ph@utq.edu.iq

Hassan A. Yasser
Physics Department, Science College, Thi-Qar University
hassan.yasser@sci.utq.edu.iq

Abstract

In this paper, a three-layer waveguide made of chiral metamaterials, separated by an interfaces of graphene, was analyzed. The mathematical formulas for the dispersion relations were derived for the hybrid odd and even modes for cases right circular polarization (RCP) and left circular polarization (LCP). Having the chiral feature will produce what are called hybrid modes. The graphene interfaces consist of three monolayers of graphene with a thickness $0.34nm$, so the thickness of the interface used is $1.02nm$. The work aims to investigate the changes that occur due to the presence of graphene material as an interface in a chiral slab waveguide. The results showed that the existence of a graphene interface in the chiral metamaterial waveguide doesn't support zero modes for odd modes. Dispersion curves may suffer from sharp changes in wavelengths at which the refractive index of graphene changes abruptly. The electric field distribution through the waveguide showed a significant effect due to the presence of graphene and the chirality property.

Keywords: slab waveguide, chiral metamaterial, graphene material, dispersion relation.

1. Introduction

Graphene is a two-dimensional atomic carbon crystal of a single layer of graphite, which can be prepared by micromechanical cleavage. Graphene has several distinctive characteristics due to its special structure, including high intrinsic strength, anomalous quantum hall effect and field effect. The optical dispersion of the refractive index is a fundamental optical property of graphene that remains unsettled [1]. An optical waveguide is a type of physical structure used to guide electromagnetic waves in the optical spectrum [2]. Three-layer slab waveguides are mathematically simple and easy to understand compared to the multiple-layer waveguides and optical fibers. However, the physical waveguide phenomena of three-layer structures are applicable to the more complicated structures. The three-layer slab waveguide is formed by three layers of dielectric material with the center layer having the largest index of refraction. The number of the guided modes that can be supported by a three layer slab waveguide depends on the thickness of the wave guiding layer and the frequency of the wave and refractive indices

[3,4]. It is worth mentioning there are various types of modes associated with slab waveguides. A trapped or bounded mode is one whose field energy is located in the neighborhood of the waveguide or center slab. The mode being a propagating wave implies that the electromagnetic energy travels along the waveguide. The electromagnetic energy stays predominantly in the high dielectric region. The other type of field satisfying Maxwell's equations is called a radiation mode. Radiation modes have field intensities that do not vanish at large distances from the slab [3].

In this work, we study a three layer slab waveguide that contains chiral metamaterial layers where a graphene sheet has been located between the two adjacent layers. Propagation equation and dispersion relations of the waveguide of even and odd modes and for both RCP (right-hand circularly polarized) waves and LCP (left-hand circularly polarized) waves are presented with some special cases that will be also mentioned.

2. Graphene Nature

The unique properties of graphene such as gate-variable optical conductivity, high-speed operation and strong coupling with light make it a very promising material for the realization of novel modulators. Graphene offers the highest intrinsic mobility and the largest current density of any material, as well as an extraordinary thermal conductivity. The surface conductivity σ, the electric field and the current density $\vec{J}$ are directly proportional to each other via the formula $\vec{J} = \sigma \vec{E}$ [5]. The graphene surface conductivity is a function of the temperature T, the chemical potential E_F, the frequency of the exciting electromagnetic wave and the diffusion rate of the carriers $\Gamma = 1/\tau$ [6]. The gate voltage V_g can dynamically adjust the conductivity of graphene because the chemical potential E_F may be controlled by an electrical gating. The Kubo formalism is typically used to calculate this conductivity, which is associated with the effects of intra-band and inter-band transitions [5,6]

$$\sigma = \sigma_{intra} + \sigma_{inter} \tag{1a}$$

$$\sigma_{intra} = -j\frac{e^2 k_B T}{\pi\hbar^2 (w - j\Gamma)}\left[\frac{E_F}{k_B T} + 2\ln\left(1 + e^{\frac{-E_F}{k_B T}}\right)\right] \tag{1b}$$

$$\sigma_{inter} = -\frac{j e^2}{4\pi\hbar}\ln\left[\frac{2|E_F| - (w - j\Gamma)\hbar}{2|E_F| + (w - j\Gamma)\hbar}\right] \tag{1c}$$

where w is the angular frequency, e is the electron change, k_B is the Boltzmann constant and $\hbar$ is the reduced Planck constant. The value of the chemical potential E_F is electrically controlled by varying the bias voltage (gate voltage V_g) on the graphene layer. The relation between chemical potential and the bias voltage is explained by the following formula [7]

$$V_g = \frac{e E_F^2 R}{\pi\hbar^2 v_F^2 \varepsilon_o \varepsilon_r} \tag{2}$$

where R is the thickness of the substrate, ε_o is the vacuum permittivity and ε_r is the substrate's relative permittivity. The relaxation time τ is defined as

$$\tau = \frac{m_o E_F}{e v_F^2} \tag{3}$$

where v_F is the Fermi velocity and m_o is the carrier mobility [8]. The mainly factors affecting graphene's optical characteristics in the THz to mid-infrared range are its carrier concentration, carrier mobility, and other electrical properties. Gating or doping can be used to control the graphene carrier concentration. The monolayer graphene's thickness is considered as $\Delta = 0.335nm$ [8,9].

3. Chiral Media

The electric and magnetic field are connected in chiral media as [10][16][17]:

$$\vec{D} = \vec{\varepsilon}\vec{E} - iK\sqrt{\varepsilon\mu}\hat{z}\hat{z}\cdot\vec{H} \tag{4a}$$

$$\vec{B} = \vec{\mu}\vec{H} + iK\sqrt{\varepsilon\mu}\hat{z}\hat{z}\cdot\vec{E} \tag{4b}$$

where $\vec{E},\vec{H},\vec{D}$ and $\vec{B}$ are the electric field, magnetic field, electric displacement and magnetic flux density, respectively. The K represents the chirality parameter, ε and μ are the permittivity and permeability of the chiral medium, $\hat{z}\hat{z}$ is dyadic tensor. Note that, the second terms in Eqs.(4) represents the coupling due to chirality. Here, the vectorial Maxwell's equations must be solved, which is a lengthy and complex process. Therefore we shall be satisfied by mentioning the coupled wave equations for the $\vec{E}$ (electric field) and $\vec{H}$ (magnetic field), namely [11]

$$\frac{\partial^2 E_z}{\partial x^2} + q^2(E_z - iK\sqrt{\mu/\varepsilon}H_z) = 0 \tag{5a}$$

$$\frac{\partial^2 H_z}{\partial x^2} + q^2(H_z + iK\sqrt{\varepsilon/\mu}E_z) = 0 \tag{5b}$$

where $q^2 = w^2\varepsilon\mu - \beta^2$ and β is the longitudinal propagation constant which can be expressed as $\beta = k_o n_{eff}$ with n_{eff} is the modal effective refractive index and $k_o = 2\pi/\lambda$ is the wave number in vacuum. Note that, Eqs.(5) shows that the two longitudinal fields are coupled by the chirality. So, the fields are generally hybrid, instead of being TE or TM modes as in the case of zero chirality where $K = 0$. The eigenfunctions that determine the hybrid nature of the modes are given by [10][18][19].

$$\begin{bmatrix} E_z \\ H_z \end{bmatrix} = \begin{bmatrix} E_z \\ \pm iE_z/\eta \end{bmatrix} \tag{6}$$

where $\eta = \sqrt{\mu/\varepsilon}$ is the medium's intrinsic impedance. In the absence of chirality, the fields are not coupled. In other words, the magnetic and electric fields are completely independent of one another. The excited fields in the specified region divide into (LCP,−) and (RCP,+) components in the presence of chirality. Electromagnetic fields in chiral media can be described as [12][20][21].

$$E_z = E_{z+} + E_{z-} \tag{7a}$$

$$H_z = H_{z+} + H_{z-} \tag{7b}$$

The magnetic and electric fields are related by

$$H_{z\pm} = \pm iE_{z\pm} / \eta \tag{8}$$

4. Theoretical Formalism

The structure used here is a symmetric slab waveguide contains a isotropic chiral metamaterial in all regions where all two adjacent layers separated by a graphene interface. Since the graphene's thickness is substantially less than the wavelength, it is thought to be an interface rather than a layer. In order to understand this structure. In the structure, the cover layer $x \geq d/2$ and the substrate layer $x \leq -d/2$ are an isotropic chiral metamaterial with parameter $\varepsilon_1, \mu_1, K_1$. The core layer $-d/2 \leq x \leq d/2$ is an another isotropic chiral metamaterial that has a permittivity ε_2, permeability μ_2, chirality parameterand thickness K_2 Fig.(1) obtains the schematic representation of the present model. . d

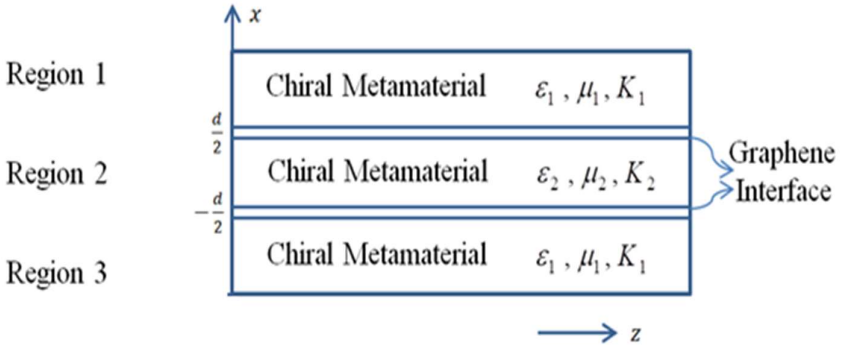

Fig. (1): Schematic of chiral metamaterial slab waveguide with graphene interfaces.

Attention that, in our derivations will separate the solutions and results on the basis of odd and even that include RCP and LCP. Therefore, for even modes, the longitudinal electric field in the three-layers take the forms

$$E_{z1} = A e^{-q_{1+}(x-h)} + B e^{-q_{1-}(x-h)} \qquad x \geq h \tag{9a}$$

$$E_{z2} = C \cos\, q_{2+} x + D \cos\, q_{2-} x \qquad -h \leq x \leq h \tag{9b}$$

$$E_{z3} = A e^{q_{1+}(x+h)} + B e^{q_{1-}(x+h)} \qquad x \leq -h \tag{9c}$$

where the parameters A, B, C and D represent the amplitudes of the waves in the different layers, $h = d/2$, $q_{1\pm} = \sqrt{\beta^2 - k_{1\pm}^2}$, $q_{2\pm} = \sqrt{k_{2\pm}^2 - \beta^2}$, $k_{i\pm} = k_o(n_{i\pm} \pm K_i)$ is the wave vector for RCP and LCP waves and n_i is the refractive index of the chiral material. Using Eqs.(7),(8) and (9), longitudinal magnetic field in the three-layer will be

$$H_{z1} = \frac{i}{\eta_1}[A e^{-q_{1+}(x-h)} - B e^{-q_{1-}(x-h)}] \qquad x \geq h \tag{10a}$$

$$H_{z2} = \frac{i}{\eta_2}[C \cos\, q_{2+} x - D \cos\, q_{2-} x\,] \qquad -h \leq x \leq h \tag{10b}$$

$$H_{z3} = \frac{i}{\eta_1}[A e^{q_{1+}(x+h)} - B e^{q_{1-}(x+h)}\,] \qquad x \leq -h \tag{10c}$$

Longitudinal components of the magnetic and electric fields are connected to the transverse

components]as [13 E_y ,H_y ,E_x ,H_x

$$E_x = -\frac{i\beta}{q^2}E_z' \tag{11a}$$

$$E_y = \frac{ik\eta}{q^2}H_z' \tag{11b}$$

$$H_y = -\frac{ik}{q^2\eta}E_z' \tag{11c}$$

$$H_x = -\frac{i\beta}{q^2}H_z' \tag{11d}$$

where the prime refers to the derivation with respect to x . The transverse components E_y ,H_y in the three layers for waveguide have the following forms using Eqs.(11):

$$E_{y1} = aA\, e^{-q_{1+}(x-h)} - bB\, e^{-q_{1-}(x-h)} \tag{12a}$$

$$E_{y2} = c\,C \sin q_{2+}x - sD \sin q_{2-}x \tag{12b}$$

$$E_{y3} = -aA\, e^{q_{1+}(x+h)} + bB\, e^{q_{1-}(x+h)} \tag{12c}$$

$$H_{y1} = \frac{ia}{\eta_1}A\, e^{-q_{1+}(x-h)} + \frac{ib}{\eta_1}B\, e^{-q_{1-}(x-h)} \tag{12d}$$

$$H_{y2} = \frac{ic}{\eta_2}C \sin q_{2+}x + \frac{is}{\eta_2}D \sin q_{2-}x \tag{12e}$$

$$H_{y3} = \frac{-ia}{\eta_1}A\, e^{q_{1+}(x+h)} - \frac{ib}{\eta_1}B\, e^{q_{1-}(x+h)} \tag{12f}$$

where $a = \frac{k_{1+}}{q_{1+}}, b = \frac{k_{1-}}{q_{1-}}, c = \frac{k_{2+}}{q_{2+}}, s = \frac{k_{2-}}{q_{2-}}$. The transmitted waves across the interfaces have the following conditions [14][22][23].

$$E_{zi} = E_{zj},\ E_{yi} = E_{yj},\ H_{zi} - H_{zj} = -\sigma E_{yi},\ H_{yi} - H_{yj} = \sigma E_{zi} \tag{13}$$

Matching the components in Eqs.(9), (10), and (12) by using the boundary conditions in Eqs.(13) across interfaces, yields

$$A + B - C\cos q_{2+}h - D\cos q_{2-}h = 0 \tag{14a}$$

$$aA - bB - c\,C\sin q_{2+}h + sD\sin q_{2-}h = 0 \tag{14b}$$

$$\eta_2 r_1 A + \eta_2 r_2 B - c\eta_1 C\sin q_{2+}h - s\eta_1 D\sin q_{2-}h = 0 \tag{14c}$$

$$\eta_2 r_3 A - \eta_2 r_4 B - \eta_1 C\cos q_{2+}h + \eta_1 D\cos q_{2-}h = 0 \tag{14d}$$

where $r_1 = a + i\sigma\eta_1$, $r_2 = b + i\sigma\eta_1$, $r_3 = 1 - ia\sigma\eta_1$, $r_4 = 1 - ib\sigma\eta_1$

To facilitate the solutions, we will unite all the functions to cos function using the following assumptions $\sin q_{2+}h = X\cos q_{2+}h$ and $\sin q_{2-}h = Y\cos q_{2-}h$,where $X = \tan q_{2+}h$, $Y = \tan q_{2-}h$, in Eqs.(14), to get

$$A + B - C\cos\ q_{2+}h - D\ \cos q_{2-}h = 0 \tag{15a}$$
$$aA - bB - cX\ C\cos\ q_{2+}h + sYD\ \cos q_{2-}h = 0 \tag{15b}$$
$$\eta_2\ r_1 A + \eta_2\ r_2 B - c\eta_1 X\ C\cos q_{2+}h - s\eta_1 YD\cos\ q_{2-}h = 0 \tag{15c}$$
$$\eta_2 r_3 A - \eta_2\ r_4 B - \eta_1\ C\cos\ q_{2+}h + \eta_1 D\cos\ q_{2-}h = 0 \tag{15d}$$

The simultaneous equations in Eqs.(15) can be solved to obtain the expressions of the unknown parameters A, B, C and D as

$$A = -B + C\cos\ q_{2+}h + D\ \cos q_{2-}h$$
$$B = \frac{c(a\eta_1 - \eta_2\ r_1)}{\eta_2\ (ar_2\ + b\,r_1)} C\sin q_{2+}h + \frac{s(a\eta_1 + \eta_2\ r_1)}{\eta_2\ (ar_2\ + b\,r_1)} D\sin\ q_{2-}h$$
$$C = \frac{\alpha_1\cos\ q_{2-}h - \alpha_2\sin\ q_{2-}h}{\alpha_3\cos\ q_{2+}h + \alpha_4\sin q_{2+}h} D, \qquad D = 1$$

where

$$\alpha_1 = (\ \eta_1 + \eta_2 r_3)\left(ar_2\ + b\ r_1\right),\ \ \alpha_2 = s\left(a\eta_1 + \eta_2\ r_1\right)\left(r_3 + r_4\right)$$
$$\alpha_3 = \left(\eta_1 - \eta_2 r_3\right)\left(ar_2\ + b\ r_1\right),\ \ \alpha_4 = c\,(a\eta_1 - \eta_2\ r_1)\left(r_3 + r_4\right)$$

The system in Eqs.(15) has a nontrivial solution, only if the determinant of the coefficients is zero. This determinant gives the following dispersion relation

$$\frac{\eta_2(r_4 + r_3)(a + sY) - (b + a)(\eta_2 r_3 + \eta_1)}{\eta_2(r_4 + r_3)(a - cX) - (b + a)(\eta_2 r_3 - \eta_1)} = \frac{\eta_2(r_2 - r_1)(a + sY) + (b + a)(\eta_2 r_1 - s\eta_1 Y)}{\eta_2(r_2 - r_1)(a - cX) - (b + a)(\eta_2 r_1 - c\eta_1 X)} \tag{16}$$

The assumption $X \neq 0, Y = 0$ can be made to calculate the dispersion equation for RCP case, and the assumption $X = 0, Y \neq 0$ can be made to calculate the dispersion equation for LCP case. Combining the two cases, will get

$$q_{2\pm}h = \tan^{-1}\left[+ \frac{k_{2\pm}}{2q_{2\pm}} \frac{\eta_1^2 + \eta_2^2 + \sigma^2\eta_1^2\eta_2^2 \mp 2\eta_1\eta_2\theta_1 + 2i\sigma\eta_1\eta_2^2\theta_2}{\eta_1\eta_2\left(\theta_3 + i\sigma\eta_1\right)} \right]^{-1} + m\pi \tag{17}$$

where $\theta_1 = \frac{k_{1+}q_{1-} - k_{1-}q_{1+}}{k_{1+}q_{1-} + k_{1-}q_{1+}}, \theta_2 = \frac{q_{1+}q_{1-} - k_{1+}k_{1-}}{k_{1+}q_{1-} + k_{1-}q_{1+}}, \theta_3 = \frac{2k_{1+}k_{1-}}{k_{1+}q_{1-} + k_{1-}q_{1+}}$

Note that, $\rho = -1$ for even modes and the signs $(+,-)$ at the sub index refer to RCP and LCP, respectively. For odd modes, in a similar manner, the boundary conditions may be applied to produce the system

$$A + B - C\sin\ q_{2+}h - D\ \sin q_{2-}h = 0 \tag{18a}$$
$$aA - bB + c\,CX\sin\ \ q_{2+}h - sD\,Y\sin\ q_{2-}h = 0 \tag{18b}$$
$$\eta_2 r_1 A + \eta_2\ r_2 B + c\eta_1\ CX\sin q_{2+}h + \eta_1 sDY\sin\ q_{2-}h = 0 \tag{18c}$$
$$\eta_2 r_3 A - \eta_2\ r_4 B - \eta_1\, C\sin\ q_{2+}h + \eta_1 D\ \sin q_{2-}h = 0 \tag{18d}$$

where $X = \cot q_{2+}h$, $Y = \cot q_{2-}h$. The last system has a non-trivial solution only for the zero determinant of the coefficient matrix. The zero determinant is exactly the dispersion equation

$$q_{2\pm}h = \tan^{-1}\left[- \frac{k_{2\pm}}{2q_{2\pm}}\ \frac{\eta_1^2 + \eta_2^2 + \sigma^2\eta_1^2\eta_2^2 \mp 2\eta_1\eta_2\theta_1 + 2i\sigma\eta_1\eta_2^2\theta_2}{\eta_1\eta_2\left(\theta_3 + i\sigma\eta_1\right)} \right]^{+1} + m\pi \tag{19}$$

where $\rho = 1$ for odd modes. The parameters A, B, C and D in this case, will be

$$A = -B + C\sin\ q_{2+}h + D\ \sin q_{2-}h$$

$$B = -\frac{c\left(a\eta_1 - \eta_2 r_1\right)}{\eta_2\left(a\,r_2 + br_1\right)} C\cos q_{2+}h - \frac{s\left(a\eta_1 + \eta_2 r_1\right)}{\eta_2\left(ar_2 + br_1\right)} D\cos q_{2-}h$$

$$C = \frac{\alpha_1 \sin q_{2-}h + \alpha_2 \cos q_{2-}h}{\alpha_3 \sin\ q_{2+}h - \alpha_4 \cos q_{2+}h} D, \qquad D = 1$$

Eqs.(17) and (19) can be combined to obtain generalized dispersion relation

$$q_{2\pm}h = \tan^{-1}\left[-\frac{\rho k_{2\pm}}{2q_{2\pm}} \frac{\eta_1^2 + \eta_2^2 + \sigma^2\eta_1^2\eta_2^2 \mp 2\eta_1\eta_2\theta_1 + 2i\sigma\eta_1\eta_2^2\theta_2}{\eta_1\eta_2\left(\theta_3 + i\sigma\eta_1\right)} \right]^{\rho} + m\pi \tag{20}$$

The last equation represents the main achievement in this work, as it represents the characteristic equation for the (RCP and LCP) odd and even modes of a slab waveguide containing chiral materials in its three layers and in the presence of graphene interfaces.

As a special cases, with no graphene interfaces, the generalized dispersion relation, i.e. Eq.(20), will be

$$q_{2\pm}h = \tan^{-1}\left[-\frac{\rho k_{2\pm}}{2q_{2\pm}} \frac{\eta_1^2 + \eta_2^2 \mp 2\eta_1\eta_2\theta_1}{\eta_1\eta_2\theta_3} \right]^{\rho} + m\pi \tag{21}$$

Furthermore, for no chiral media in the covering layers, $k_{1\pm} = k_1, q_{1\pm} = q_1$, such that Eq.(21) reduces to the simple form

$$q_{2\pm}h = \tan^{-1}\left[-\frac{\rho}{2} \frac{k_{2\pm}q_1}{q_{2\pm}k_1} \frac{\eta_1^2 + \eta_2^2}{\eta_1\eta_2} \right]^{\rho} + m\pi \tag{22}$$

For chiral covering layers, non-chiral core layer and without graphene interfaces, Eq.(20) will be

$$q_2h = \tan^{-1}\left[-\frac{\rho k_2}{2\,q_2} \frac{\eta_1^2 + \eta_2^2 \mp 2\eta_1\eta_2\theta_1}{\eta_1\eta_2\theta_3} \right]^{\rho} + m\pi \tag{23}$$

Here, the signs (m) are the result of the mathematical derivation, where we get the sign (+) in the case of $X = 0$ and $Y \neq 0$, while the sign $(-)$ in the case of $X \neq 0$ and $Y = 0$.

5. Results and Discussion

In this section, we will take a three-layer chiral metamaterial waveguide with graphene interfaces with a thickness $1.02nm$ and the parameters $v_F = 1\times10^6 m/s\ m_o = 8\times10^4 cm^2/sV$ and $T = 300K^o$ to simulate the conductivity, permittivity and refractive index of graphene material. The parameters used to simulate the dispersion relations of guided modes of slab waveguide with graphene interface are $E_F = 1eV$, $\varepsilon_1 = \mu_1 = 1,\ \varepsilon_2 = \mu_2 = -3.5$ and core thickness $d = 1\mu m$. Other parameters will be imposed during the simulation.

Fig.(2) represents the real and imaginary part of permittivity as function of the chemical potential E_F for a range of different wavelengths. We note that the real part of permittivity starts with a positive increase, which means that the graphene layers show insulator properties, then the dielectric function turns to become negative, this means that the graphene will change

from an insulator state to a metallic behavior. The imaginary part at the beginning is fixed at a certain value for each wavelength and then a drop occurs sudden. The epsilon near zero (ENZ) point is where the permittivity of graphene approaches zero at a chemical potential E_F is around $0.5eV$ at $\lambda = 1.8\,\mu m$. When E_F greater than $0.5eV$, the imaginary part of permittivity has a smaller absolute magnitude then the real part of permittivity. Surface plasmons can propagate on the graphene substrate under these circumstances [15].

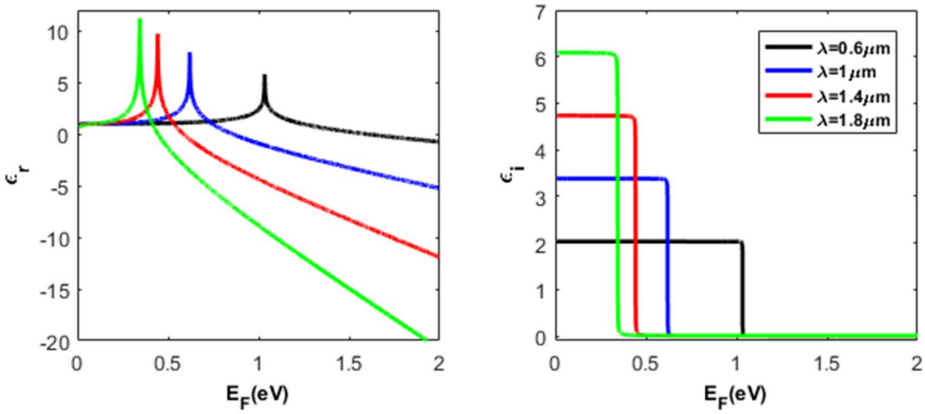

Fig.(2): real and imaginary parts of permittivity as functions of chemical potential for many wavelengths.

The change in the real and imaginary parts of conductivity as function of wavelength is seen in Fig.(3), for chemical potential $E_F = (0.25, 0.5, 0.75, 1)eV$. The real conductivity has a sharp drop while the imaginary part starts from zero, after that it decreases to negative values. At $\lambda > 0.6\,\mu m$, the imaginary part returns to take large positive values of about $200\,\mu S$. In general, the decrease in conductivity is greater when the E_F is large, since the lowest decrease is at $E_F = 0.25eV$ and $\lambda = 2.5\mu m$. when E_F increases, the characteristics of the real and imaginary parts of the conductivity (the spike and the abrupt fall dot) exhibit a rapid green shift in range $\lambda = (0-3)\mu m$.

As a function of the number of graphene layers for various wavelengths at $E_F = 0.5eV$, the real and imaginary parts of refractive index are shown in Fig.(4). Despite the differing wavelength, the refractive index shows a distinct drop for both the real and imaginary parts with an increase in the number of layers. When compared to the imaginary part of refractive index, the real part has the highest value for a single layer. Noting that the number of layers is affects thickness, therefore changing the number of layers (either increasing or decreasing) gives flexibility to control the thickness for graphene interface. As a result, can be said that the refractive index for multilayered graphene decreases with increased the thickness.

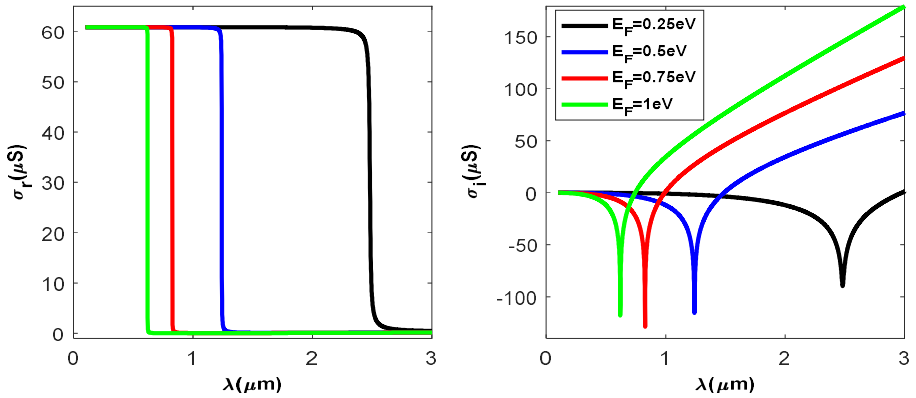

Fig.(3): real and imaginary parts of conductivity as function of wavelengths for many chemical potential.

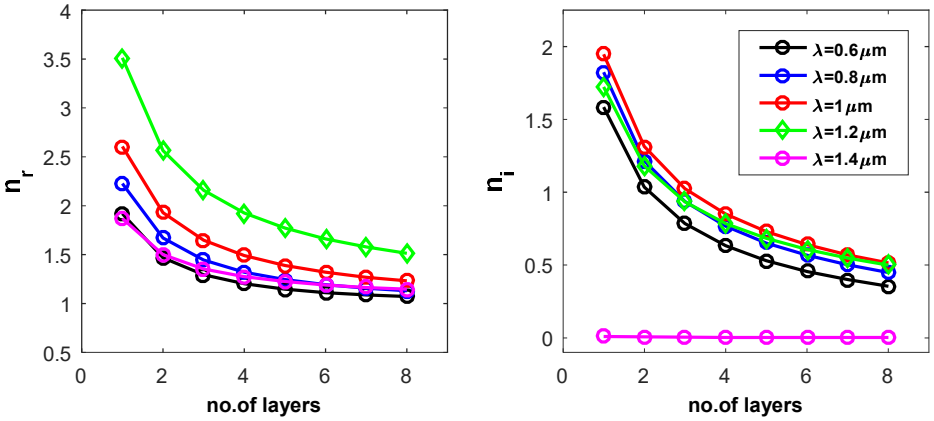

Fig.(4): real and imaginary parts of refractive index as functions of number of layers for many wavelengths at $E_F = 0.5eV$.

Figs.(5) and (6) corresponds to the variation of effective refractive index n_{eff} against the normalized frequency parameter $k_o d$ at $K_1 = 0.2$ for odd and even modes, respectively. In the figures, the solid blue line indicates the state LCP, while the red dashed line represents the RCP state. For non-chiral waveguide ($K_2 = 0$), we observe that the values of effective refractive index n_{eff} of blue and red modes match each other of the same order with increasing normalized frequency $k_o d$. Since neither right-circularly polarized (RCP) nor left-circularly polarized (LCP) waves exist in this type of waveguide, transverse magnetic modes TM instead occur instead of hybrid modes. For chiral waveguide ($K_2 = 0.2$), the RCP and LCP modes of the same order diverge as the normalized frequency $k_o d$ increases. The red lines (RCP) in the case $K_2 = 0.2$ have higher values of effective refractive index compared to the case LCP, and the blue lines (LCP) have a smaller backward propagation. Even modes start with $m = 1$, while odd modes with $m = 0$, then higher-order modes appear with increasing normalized frequency $k_o d$, so the backward propagation turns into forward with increasing $k_o d$.

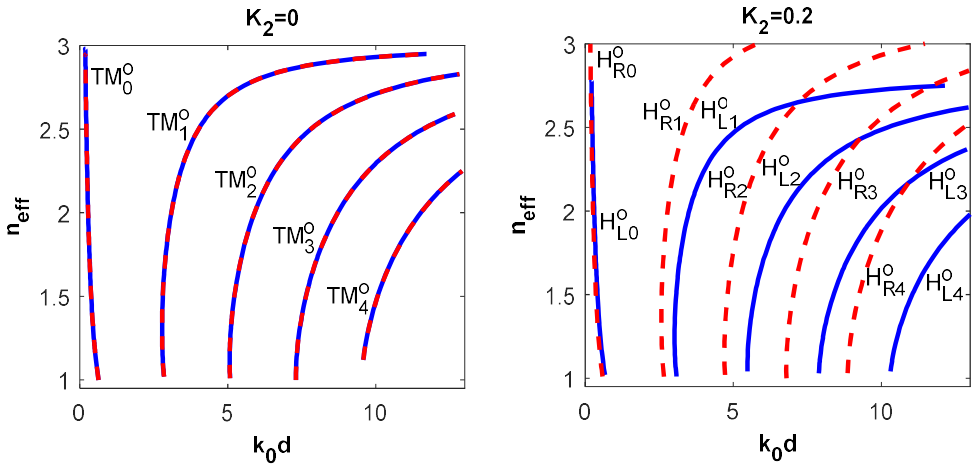

Fig.(5): the dispersion relation for odd modes at $K_1 = 0.2$, where the red and blue lines represent the case RCP and LCP, respectively.

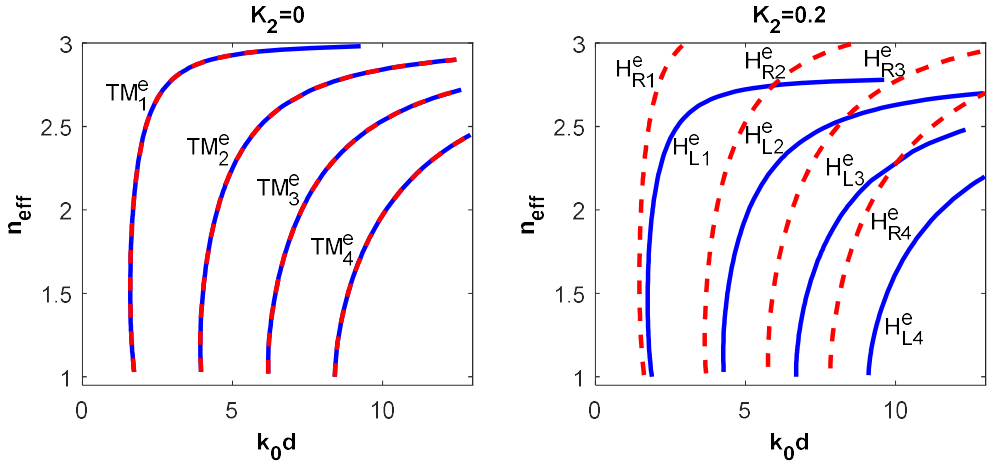

Fig.(6): the dispersion relation for even modes at $K_1 = 0.2$, where the red and blue lines represent the case RCP and LCP, respectively.

Fig.(7) represent the dispersion relations of guided modes at $K_2 = 0.2$ in chiral metamaterial core slab waveguide. Blue color refers to odd modes while red color shows even modes. The chiral metamaterial is in the core and cladding regions where the chirality parameter for two layers is $K_1 = K_2 = 0.2$. We note that even modes begin first and then followed by odd modes, as well as, the effective refractive index increases significantly in case LCP compared to the RCP (relative increase) with increasing normalized frequency $k_o d$. The zero mode takes different behavior either the remaining modes they appear increases in order with high frequencies. For both RCP and LCP, first hybrid mode gets the highest values for effective refractive index compared to other modes that have a backward propagation.

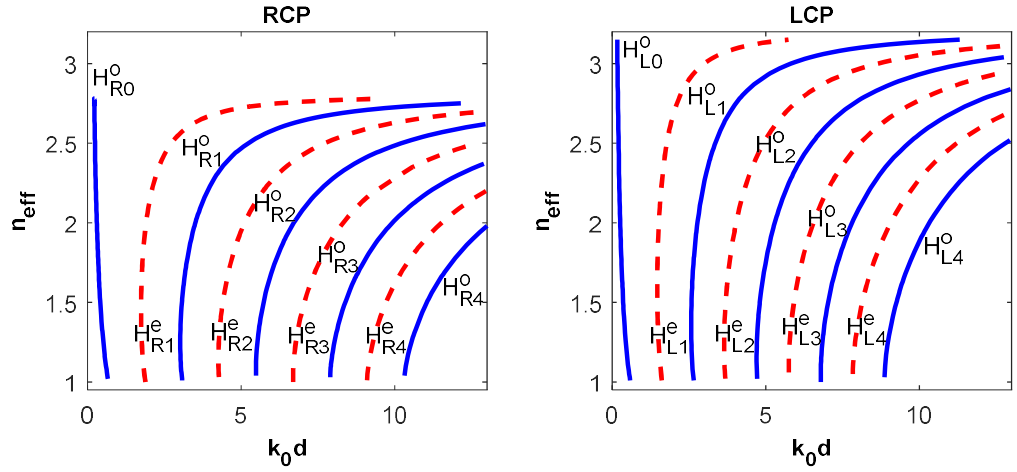

Fig.(7): the dispersion relation at $K_1 = K_2 = 0.2$, where the blue and red lines represent the case odd and even modes, respectively.

Figs.(8) and (9) show dispersion relations of odd and even modes in chiral metamaterial core slab waveguide has chirality parameter $K_2 = 0.2$ and $K_1 = 0$, respectively. The characteristic curves of the two cases: the presence of conductivity (red color) and the absence of conductivity (blue color) are presented in order to clarify the effect of graphene material on the chiral waveguide as an interface. In the case $\sigma \neq 0$, the zero mode doesn't appear, which indicates that the graphene interface in the chiral waveguide doesn't support zero modes. For modes $H^o_{R1}, H^o_{L1}, H^e_{R1}, H^e_{L1}$, are completely identical in both cases, but there is a slight difference in the modes $H^o_{R2}, H^o_{L2}, H^e_{R2}, H^e_{L2}$, this difference becomes more obvious with increase mode order and normalized frequency $k_o d$ Compared to LCP case, the RCP case is more affected by the presence of graphene. Generally, the effective refractive index increases with increasing normalized frequency $k_o d$, but in the case $\sigma \neq 0$, it doesn't need higher frequencies compared to the other case.

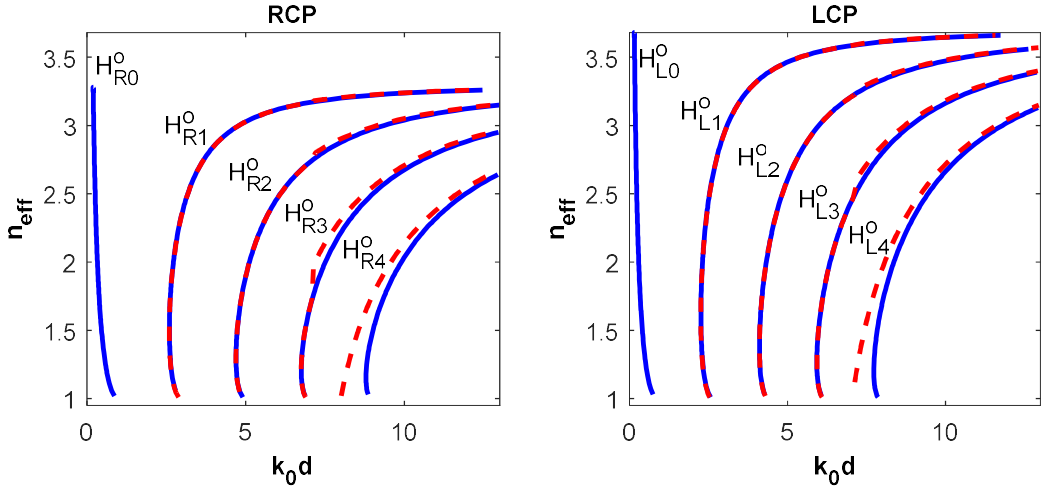

Fig.(8): the dispersion relation for odd modes at $K_2 = 0.2$, where the blue

and red lines represent the case $\sigma = 0$ and $\sigma \neq 0$, respectively.

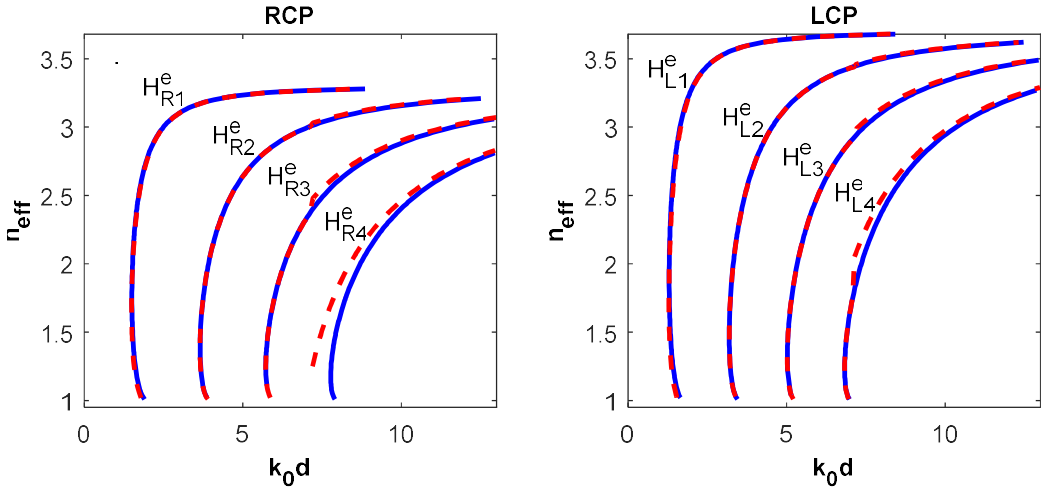

Fig.(9): the dispersion relation for even modes at $K_2 = 0.2$, where the blue and red lines represent the case $\sigma = 0$ and $\sigma \neq 0$, respectively.

Figs.(10) and (11) illustrates dispersion relation of guided modes (odd and even, respectively) at $K_1 = K_2 = 0.2$ of chiral slab waveguide. We have used different values of the dielectric constants for the central region in the waveguide, as a result, we have three different cases: the first case $\varepsilon_2 = \mu_2 = -2.5$ at is indicated in blue color, the second case at $\varepsilon_2 = \mu_2 = -3$ is represented in red color and the third case at $\varepsilon_2 = \mu_2 = -3.5$ is green color. For blue lines, we get lower values of effective refractive index within a larger normalized frequency range. Red lines have somewhat higher effective refractive index values and lower normalized frequencies. Compared to other cases, green lines have the highest effective refractive index values and very low normalized frequency range. In general, the effective refractive index values typically increase as the values of the dielectric constants increase. This means that the relation between them is a direct proportion.

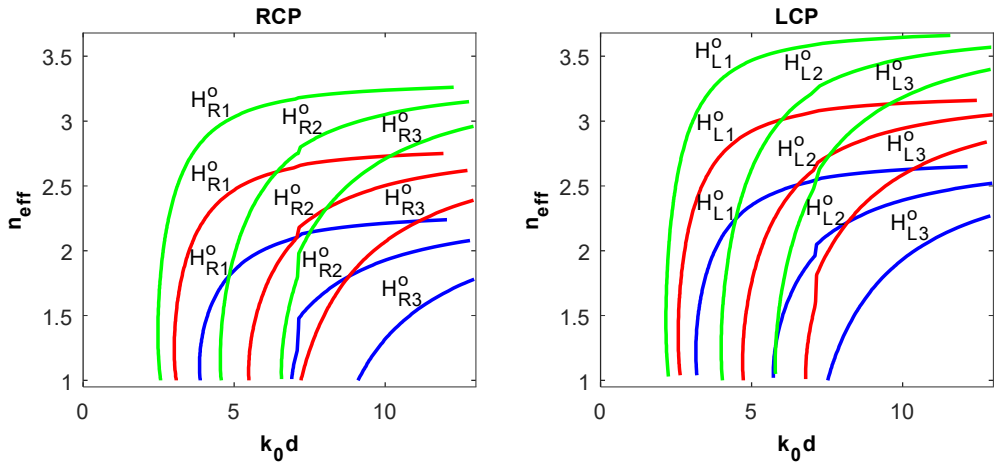

Fig.(10): the dispersion relation for odd modes at $K_1 = K_2 = 0.2$, for various core permittivity and permeability.

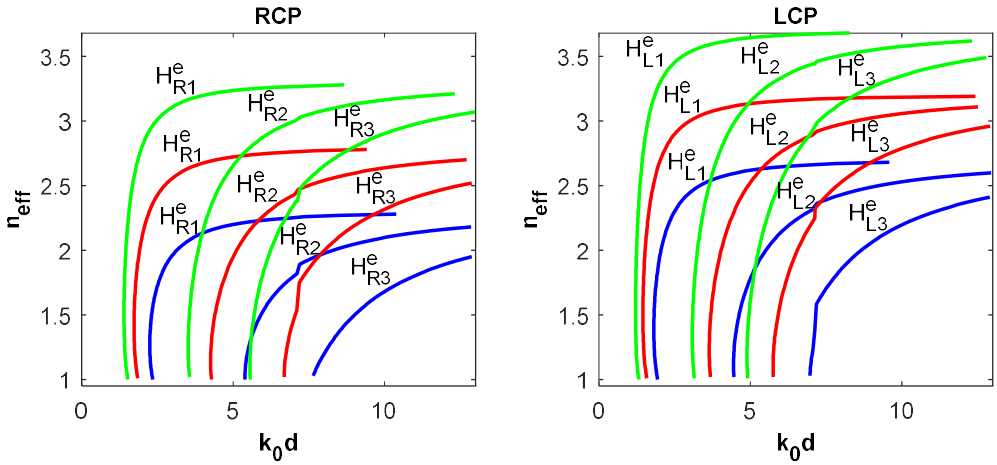

Fig.(11): the dispersion relation for even modes at $K_1 = K_2 = 0.2$, for various core permittivity and permeability.

Figs.(12) and (13) show the distribution of amplitude of electric field component E_z of odd guided modes in two cases, the absence and presence of graphene interface, respectively. The lines in the figures are: black lines representing the interface graphene, blue lines representing the tenth pair of mode $m = 1$ (specific point that achieves a backward propagation) and red lines representing the thirtieth pair of mode $m = 1$ (specific point that achieves a forward propagation). These pairs were chosen in order to learn more about the characteristics of the electric field distribution. When the conductivity value is raised, we observe that there is a significantly change in the red lines. This means that the presence of graphene causes a reduction in the effect of forward propagation compared to the backward propagation in the core region. The figures show an exponential decrease in the cladding medium and oscillatory behavior in the guiding film. The field that results from forward propagation has positive and negative values in the chiral metamaterial core and is always positive in the layers around it. In the surrounding layers, the field caused by backward propagation is high and positive, while in the core layers, it is negative. At $\sigma = 0$, the backward propagation field of case RCP exhibits unusual behavior as it has negative values in the cladding layers compared to the remaining cases.

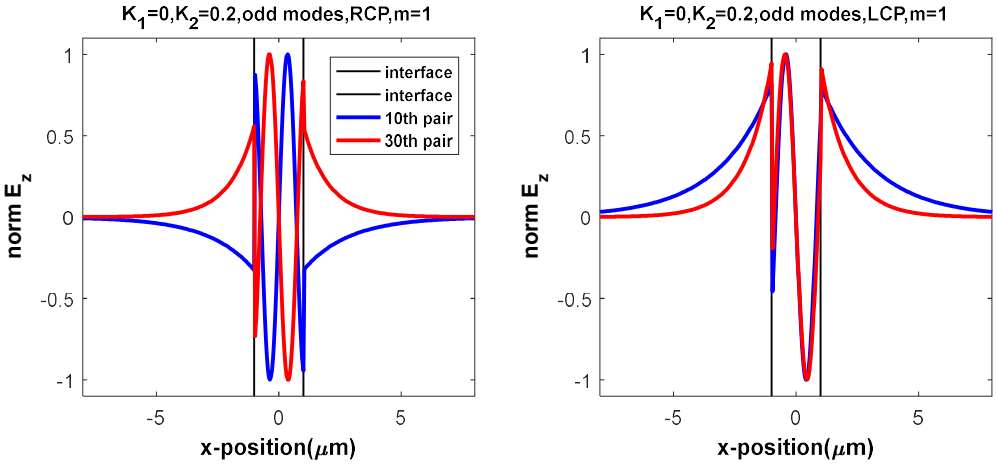

Fig.(12): the electric field distribution for odd modes in the waveguide layers with $\sigma = 0$.

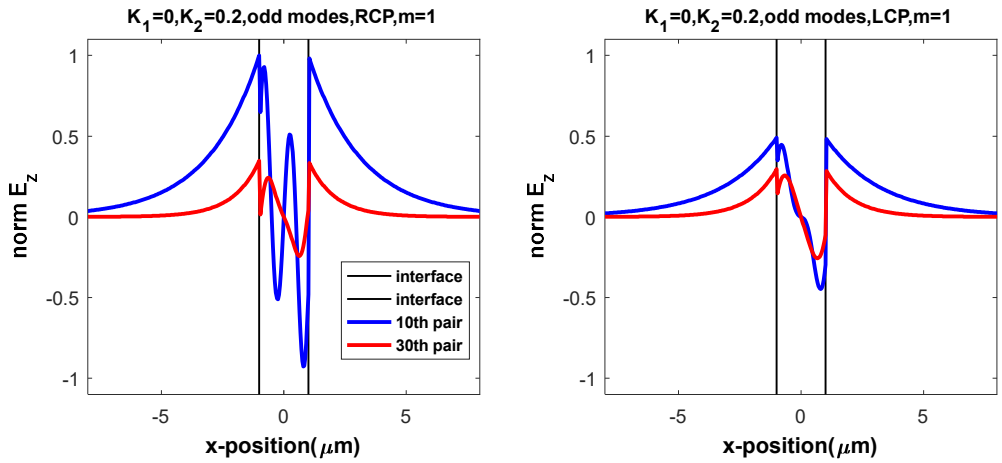

Fig.(13): the electric field distribution for odd modes in the waveguide layers with $\sigma \neq 0$.

Figs.(14) and (15) show how the electric field distribution of even guided modes varies with distance in the waveguide in the case of $\sigma = 0$ and $\sigma \neq 0$, respectively. The electric field oscillates in the guiding layer and is evanescent in the surrounding media. The two tails of the evanescent are symmetric in the substrate and cladding due to the symmetric structure assumed. The fields in the guiding layer are always positive and large, while the fields in the cladding layers have negative values.

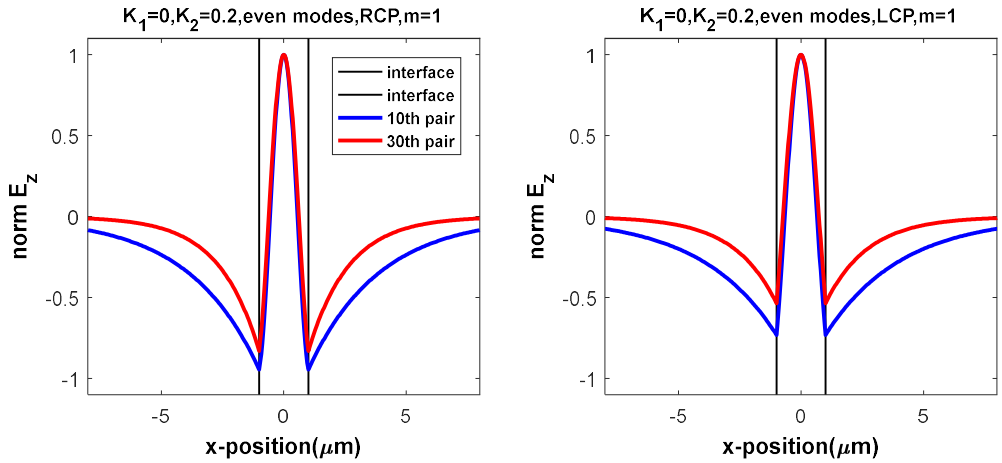

Fig.(14): the electric field distribution for even modes in the waveguide layers with $\sigma = 0$.

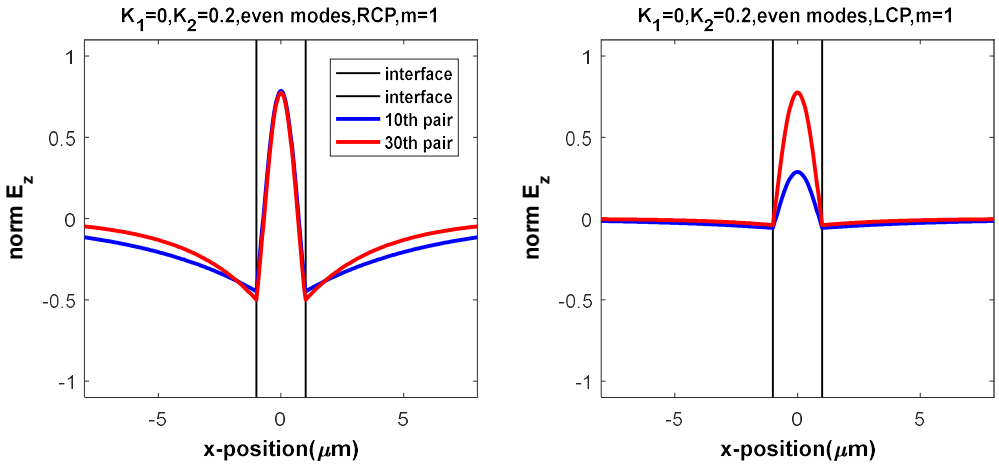

Fig.(15): the electric field distribution for even modes in the waveguide layers with $\sigma \neq 0$.

6. Conclusions

As a conclusion, the graphene may be changed from insulator state to a metallic behavior depending of wavelength and E_F. When the chemical potential is high, the decrease in conductivity is larger and the effective refractive index for multilayered graphene decreases as the thickness increases. There may be unique property introduced by the presence of graphene interfaces that is distinct from that of a conventional waveguide. The effect of chiral metamaterial on the mode increases as the chiral metamaterial core region thickness increases, which in turn causes divergence of modes for the same order. As the values of the dielectric constants increases, the values of the effective refractive index often rise. In the guiding film, the electric field distribution exhibits oscillatory behavior, while in the cladding medium, it exhibits exponential decay.

References

[1] X. Wang, Y. Chen and D. Nolte, "Strong Anomalous Optical Dispersion of Graphene: Complex Refractive Index Measured by Picometrology", Optics Express, pp.1-14, 2009.

[2] W. Wong-Ng and C. Rawn, "Crystallography of Functional Materials", Crystals, Vol.7, No.279, pp.1-6, 2017.

[3] H. Kress and J. Butler, "Semiconductor Lasers and Heterojunction LEDs", Academic Press, 1977.

[4] N. Fawaz and A. Hameed, "Wave Propagation in Dielectric Slab Waveguide with two Different Cladding Materials", Journal of University of Anbar for Pure Science, Vol.7, No.1, 2013.

[5] J. Gosciniak and D. Tan, "Graphene-Based Waveguide Integrated Dielectric-Loaded Plasmonic Electro-Absorption Modulators", Nanotechnology, Vol.24, No.185202, pp.1-9, 2013.

[6] M. Azizi1, M. Ksiksi1, H. Ajlani and A. Gharsallah, "Terahertz Graphene-Based Reconfigurable Patch Antenna", Progress In Electromagnetics Research Letters, Vol.71, pp.69–76, 2017.

[7] M. Gatte, P. Soh, H. Rahim, R. Ahmad and M. Malek, "The Performance Improvement of

THz Antenna via Modeling and Characterization of Doped Graphene", Progress In Electromagnetics Research M, Vol.49, pp.21–31, 2016.
[8] S. Asgari and T. Fabritius, "Equivalent circuit model of graphene chiral multi-band metadevice absorber composed of U-shaped resonator array", Optics Express, Vol.28, No.26, 2020.
[9] Y. Wang, H. Liu, S. Wang, M. Cai and L. Ma, "Optical Transport Properties of Graphene Surface Plasmon Polaritons in Mid-Infrared Band", Crystals, Vol.9, No.354, 2019.
[10] M. Baqir and P. Choudhury, "On The Energy Flux Through a Uniaxial Chiral Metamaterial Made Circular Waveguide Under PMC Boundary", Journal of Electromagnetic Waves and Applications, Vol. 26, No.16, pp.1-11, 2012.
[11] M. Baqir and P. Choudhury, "On the energy flux through a uniaxial chiral metamaterial made circular waveguide under PMC boundary", Journal of Electromagnetic Waves and Applications, pp.1-11, 2012.
[12] A. Helal, S. Taya and K. Elwasife, "Propagation of Electromagnetic Waves in Slab Waveguide Structure Consisting of Chiral Nihility Claddings and Negative-Index Material Core Layer", Photonic Sensors, Vol.8, No.2, pp.176-187, 2018.
[13] M. Abadla and S. Taya, "Theoretical investigation of guided modes in planar waveguides having chiral negative index metamaterial core layer", Optik-International Journal for Light and Electron Optics, pp.1-20, 2016.
[14] C. Balanic, "Advanced Engineering Electromagnetics", John Wiley and Sons, 1989.
[15] G. Jacob, G. Raina, "Frequency Dependent Graphene Surface Plasmon Properties on Different Dielectrics", International Journal of Recent Technology and Engineering, Vol.8, 2019.
[16] Narayan, Vipul, and A. K. Daniel. "Energy Efficient Protocol for Lifetime Prediction of Wireless Sensor Network using Multivariate Polynomial Regression Model." Journal of Scientific & Industrial Research 81.12 (2022): 1297-1309.
[17] Choudhary, Shubham, et al. "Fuzzy approach-based stable energy-efficient AODV routing protocol in mobile ad hoc networks." Software Defined Networking for Ad Hoc Networks. Cham: Springer International Publishing, 2022. 125-139.
[18] Narayan, Vipul, and A. K. Daniel. "RBCHS: Region-based cluster head selection protocol in wireless sensor network." Proceedings of Integrated Intelligence Enable Networks and Computing: IIENC 2020. Springer Singapore, 2021.
[19] Narayan, Vipul, and A. K. Daniel. "CHOP: Maximum coverage optimization and resolve hole healing problem using sleep and wake-up technique for WSN." ADCAIJ: Advances in Distributed Computing and Artificial Intelligence Journal 11.2 (2022): 159-178.
[20] Narayan, Vipul, and A. K. Daniel. "CHHP: coverage optimization and hole healing protocol using sleep and wake-up concept for wireless sensor network." International Journal of System Assurance Engineering and Management 13.Suppl 1 (2022): 546-556.
[21] Narayan, Vipul, and A. K. Daniel. "IOT based sensor monitoring system for smart complex and shopping malls." Mobile Networks and Management: 11th EAI International Conference, MONAMI 2021, Virtual Event, October 27-29, 2021, Proceedings. Cham: Springer International Publishing, 2022.
[22] Narayan, Vipul, et al. "E-Commerce recommendation method based on collaborative filtering technology." International Journal of Current Engineering and Technology 7.3 (2017):

974-982.
[23] Vipul, Narayan, and A. K. Daniel. "A novel protocol for detection and optimization of overlapping coverage in wireless sensor network." International Journal of Engineering and Advanced Technology 8.6 (2019): 422-462.